International Journal of Refrigeration 149 (2023) 35–48

Contents lists available at ScienceDirect

International Journal of Refrigeration

journal homepage: www.elsevier.com/locate/ijrefrig

Investigations on the coupling principle of the four-stage DC linear compressor unit used in a hybrid cryocooler operating in 1–2 K

Études sur le principe de couplage du groupe compresseur linéaire à courant continu à quatre étages utilisé dans un cryoréfrigérateur hybride fonctionnant à 1-2 K

Yongjiang Zhao [a,c], Jun Tan [a], Bangjian Zhao [a,c], Han Tan [a,c], Renjun Xue [a,c], Shiguang Wu [a,c], Yujia Zhai [a,c], Dirui Wu [a,c], Dong Ma [a,c], Haizheng Dang [a,b,c,d,*]

[a] State Key Laboratory of Infrared Physics, Shanghai Institute of Technical Physics, Chinese Academy of Sciences, 500 Yutian Road, Shanghai 200083, China
[b] Shanghai Research Center for Quantum Sciences, Shanghai, 201315, China
[c] University of Chinese Academy of Sciences, Beijing, 100049, China
[d] Shanghai Boreas Cryogenics Co., Ltd, Shanghai, 201802, China

ARTICLE INFO

Keywords:
Four-stage DC linear compressor unit
Coupling principle
Equivalent non-linear dynamic model
1–2 K hybrid cryocooler
Experimental verification

Mots clés:
Groupe compresseur linéaire à courant continu à quatre étages
Principe de couplage
Modèle dynamique non linéaire équivalent
Cryoréfrigérant hybride 1-2 K
Vérification expérimentale

ABSTRACT

In a hybrid cryocooler developed for operating in 1–2 K, a four-stage DC linear compressor (DCLC) unit used in a Joule-Thomson cooler (JTC) is designed to provide the extremely low suction pressure of below 3.1 kPa. An equivalent non-linear dynamic model is proposed to analyze the gas spring force within the cylinder, and the coupling principles among stages of the DCLC unit are analyzed and summarized for the optimal design. In a standalone test platform, the experimental results show that the designed four-stage DCLC unit can provide a suction pressure of 2.1 kPa, for which a total pressure ratio (TPR) of 102.5 is reached with a pressure ratio loss (PRL) of 13.4%. Furthermore, in the actual hybrid cryocooler, the acquired values of suction pressure, TPR and PRL are 1.75 kPa, 101.7 and 14.1%, respectively, which is of great significance for the hybrid cryocooler in achieving 1.8 K. The rationality and feasibility of the coupling principle are experimentally verified.

1. Introduction

The single photon detector (SPD) plays an important role in the space quantum information technology (Cozzolino et al, 2019). The superconducting nanowire SPD (SNSPD) with high detection efficiency, low dark count rate and high detection speed is attractive in the future applications (You, 2020), however, it requires a very low temperature (usually around 2 K) to normally work, which is an enormous challenge to the refrigeration technology (Radebaugh, 2009; Ross, 2007). In the authors' laboratory, a hybrid cryocooler which incorporates a four-stage Stirling-type pulse tube cryocooler (SPTC) as the precooling stage and a Joule-Thompson cooler (JTC) as the terminal stage is being developed, which has achieved a no-load temperature of 1.8 K with He-4 as the only working medium in the whole system (Dang et al, 2022). As the terminal stage in the hybrid cryocooler operating at such a low temperature, the JTC must be subjected to several stringent requirements. For example, the suction pressure after the throttling valve is a critical factor which determines the theoretical minimum temperature achieved by the JTC. In order to reach a temperature of below 2 K with He-4, the pressure must be lower than 3.1 kPa, which is a formidable challenge for the close-cycle compressor (Zhang and Dang, 2021). Furthermore, considering the potential space applications, either rotary or scroll compressor is excluded, while the Oxford-type moving-coil linear compressor originally developed for the SPTCs in the authors' laboratory becomes an appropriate option. However, a suction and a discharge valve must be introduced to the original compressor to provides a DC flow (Liang, 2017). Such a compressor is defined here as the DC linear compressor

* Corresponding author at: State Key Laboratory of Infrared Physics, Shanghai Institute of Technical Physics, Chinese Academy of Sciences, 500 Yutian Road, Shanghai 200083, China.
E-mail address: haizheng.dang@mail.sitp.ac.cn (H. Dang).

https://doi.org/10.1016/j.ijrefrig.2022.12.020
Received 21 October 2022; Received in revised form 20 December 2022; Accepted 21 December 2022
Available online 24 December 2022
0140-7007/© 2022 Elsevier Ltd and IIR. All rights reserved.

Nomenclature

A_p	cross-sectional area of piston (m^2)
B	magnetic field strength (T)
C	coefficient of viscous friction ($kg{\cdot}s^{-1}$)
CV	control volume
D_b	equivalent diameter of CV (m)
DCLC	DC linear compressor
F	static force (N)
$\vec{F_s}$	mechanical spring force (N)
$\vec{F_r}$	viscous frictional resistance (N)
$\vec{F_a}$	inertial force (N)
$\vec{F_g}$	gas spring force (N)
$\vec{F_e}$	motor force (N)
F	frequency (Hz)
G	mass flow rate ($kg{\cdot}s^{-1}$)
H	hysteresis factor ($kg{\cdot}s^{-1}$)
I	current (A)
JTC	Joule-Thomson cooler
k_g	gas spring stiffness factor ($N{\cdot}m^{-1}$)
k_s	flexure spring stiffness factor ($N{\cdot}m^{-1}$)
K_r	local resistance factor
L	length of wire in coil (m)
M	mass of moving part (kg)
N	adiabatic coefficient
PRL	pressure ratio loss
R	resistance of single-sided coil (Ω)
Re	Reynolds number
S	stroke (m)
SPTC	Stirling-type pulse tube cryocooler
TPR	total pressure ratio
x	displacement of piston (m)
X	position of piston (m)

Greeks

α	pressure ratio
θ	phase angle of thermodynamic states
ρ	density of medium ($kg{\cdot}m^{-3}$)
ω	angular velocity of piston displacement

Subscripts

b	backside of piston
c	cylinder
eq	equivalent
h	high pressure (discharge pressure)
l	low pressure (suction pressure)
S	static equilibrium position
0	dynamic equilibrium position
$1,2$	thermodynamic states in Fig. 4

(DCLC).

For the compressors in the JTC, besides the extremely low suction pressure, a high enough pressure before the throttling valve is also essential to obtain the necessary cooling power. The multi-stage DCLC unit is often proposed to solve the problem, which means applying multiple DCLCs with different structural parameters connected in series to get a higher pressure ratio (Barta et al, 2021). For example, Sato et al (2016) developed a 1 K-class JT cryocooler using the four-stage linear compressors as the JT compressor system which provided a He-3 flow at absolute pressure from 7 to 700 kPa. And Crook M. et al. (Crook et al, 2021) also reported a 2 K JTC using the four-stage linear compressors to provide a He-3 flow from 15 to 800 kPa. In this paper, a four-stage DCLC unit with a pressure ratio of over 100 and a suction pressure of lower than 3.1 kPa is introduced, and an equivalent non-linear dynamic model will be proposed to analyze the gas force within the cylinder. The coupling principle among stages of the DCLC unit will be focused on to achieve the optimal design, and the corresponding experimental verifications will be presented.

2. The physical model of the piston in the DCLC

2.1. Structure of the Oxford-type moving-coil DCLC

Fig. 1 shows the structure of a typical DCLC based on the Oxford-type moving-coil compressor developed in the authors' laboratory (Dang et al, 2016) which adds a suction valve and a discharge valve to realize the DC flow. The dynamic characteristics of the piston are closely related to the electromagnetic force, the elastic force of the flexure spring, the gas force, and the gas state parameters of the inlet and outlet. A study on the characteristics will provide the guidance for the coupling analysis of the multi-stage DCLC unit.

2.2. Dynamic model of the piston during stable operation process

Fig. 2 shows the dynamic model of the piston in a DCLC. During the steady operation process, the piston makes a harmonic form of reciprocating motion between the top dead center and the bottom dead

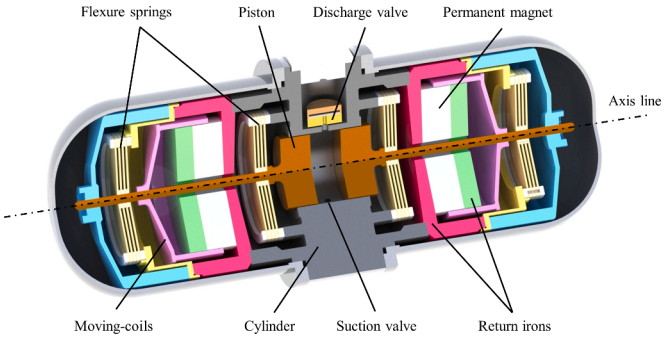

Fig. 1. Schematic of a typical Oxford-type moving-coil DCLC.

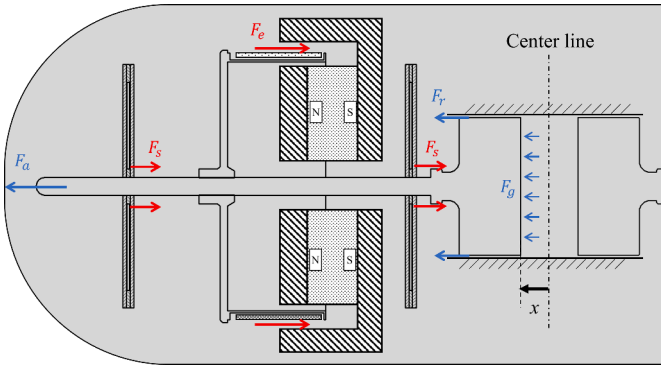

Fig. 2. Dynamic model of the piston in the DCLC.

center, and the equation of motion can be expressed as:

$$x(t) = X_0 + \frac{S}{2}\cos\omega t \tag{1}$$

where x is the piston displacement, and the zero point is selected to be the center position of the compression chamber, X_0 is the dynamic equilibrium position of the motion, S is the stroke and ω is the angular velocity of the motion. The center position of motion of the piston is not a fixed value only determined by the mechanical structure, but is more sensitive to the motor forces and gas force instead, which in turn affects the pressure ratio of the compressor.

According to the dynamic model in Fig. 2, the forces on the piston are all in the axial direction, and its equilibrium equation is (Dang et al, 2016):

$$\overrightarrow{F_s} + \overrightarrow{F_r} + \overrightarrow{F_a} - \overrightarrow{F_g} = \overrightarrow{F_e} \tag{2}$$

The corresponding control equation is:

$$k_s[x(t) - X_s] + C\dot{x}(t) + m\ddot{x}(t) - f_g(t) = BLi(t) \tag{3}$$

where X_s is the static equilibrium position ($X_s \neq X_0$), C is the resistance coefficient of the clearance seal between the piston and the cylinder. The gas force f_g is generated by the pressure difference between the cylinder and the pressure on the backside of the piston. During steady operation, the gas pressure on the backside of the piston can be regarded as a fixed value and the function of gas force is similar to the flexure springs, and is therefore also called the gas spring force. The definition of the gas spring force is given by (Zhang et al, 2019):

$$f_g(t) = A_p[P_c(t) - P_b] \tag{4}$$

where A_p is the cross-sectional area of the piston, P_b is the pressure on the backside of the piston and P_c is the value of the pressure in the cylinder, which can be determined by the P-V diagram of the cylinder shown in Fig. 3.

There are two isobaric and two adiabatic processes in a whole cycle under the ideal conditions (Zhu et al, 2022), and the pressure of cylinder can be expressed as follows:

$$P_c(t) = \begin{cases} P_l\left[\dfrac{X_0 + S/2}{x(\omega t)}\right]^n & \omega t \in (\theta_1, \theta_2) \\ P_h & \omega t \in (\theta_2, \theta_3) \\ P_h\left[\dfrac{X_0 - S/2}{x(\omega t)}\right]^n & \omega t \in (\theta_3, \theta_4) \\ P_l & \omega t \in (\theta_4, \theta_1 + 2\pi) \end{cases} \tag{5}$$

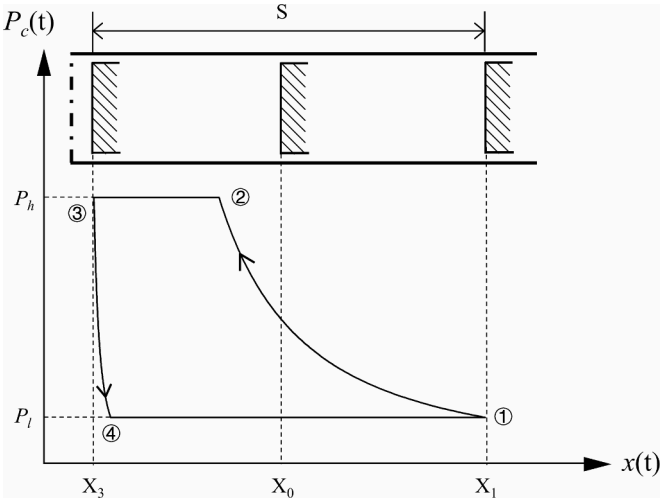

Fig. 3. P-V curve and the position of the piston in the cylinder in a cycle.

where P_h is the pressure outside the discharge valve, P_l is the pressure outside the suction valve, n is the adiabatic coefficient of the working medium.

By combining Eqs. (1) to (5), the equations for controlling the motion of the piston within a DCLC can be obtained. The gas force f_g is not a linear relationship with the motion, which makes the P-V curve of the piston to present a non-linear characteristic. Moreover, the non-linear characteristics are more apparent with the increasing of pressure ratio (Liang, 2018).

2.3. Equivalent non-linear dynamic model of the piston

In the dynamic model, the gas spring force is the only non-linear term in the equation. With Eqs. (4) and (5) alone, the control equation for the piston cannot be determined, making it difficult to design and evaluate the structural parameters of the compressor by the control equation. However, in the steady process, the piston motion can be considered as a standard harmonic motion shown in Eq (1). For the piston in this state, an equivalent harmonic function with higher order can be simulated to replace the non-linear gas force in Eq. (4), which is called the equivalent non-linear dynamic model (Choe and Kim, 2000).

The gas force can be divided into three parts according to its source. The first part is the static pressure during the reciprocating motion, which is proportional to the displacement of the piston. The second part is the viscous resistance of the gas, which is proportional to the velocity of the piston. And the third part is a static force caused by the difference between the average pressure of the cylinder and the one backside of the piston, which is a fixed value. And thus the gas force can be expressed as follows:

$$f_{g,eq}(t) = k_{eq}y(\omega t) - \frac{h_{eq}}{\omega}y(\dot{\omega t}) + F_{eq} \tag{6}$$

where

$$y(t) = x(\omega t) - X_o = \frac{S}{2}\cos\omega t \tag{7}$$

where k_{eq}, h_{eq} and F_{eq} are the equivalent spring stiffness factor, the equivalent hysteresis factor and the equivalent static force, respectively. Note that the actual gas force is still controlled by Eqs. (4) and (5) and the equivalent gas force represented by Eq. (6) is an equivalent harmonic function with the same integration result as the actual gas force mathematically.

Substituting Eqs. (6) and (7) back into Eq. (3), the control equation under the equivalent model is obtained as follows:

$$m\frac{d^2y(\omega t)}{dt^2} + \left(C + \frac{h_{eq}}{\omega}\right)\frac{dy(\omega t)}{dt} + (k + k_{eq})y(\omega t) - \left[k(X_s - X_0) + F_{eq}\right] = BLi(\omega t) \tag{8}$$

Since y(t), i(t) are harmonic functions, Eq. (8) can be further decomposed as:

$$m\frac{d^2y(\omega t)}{dt^2} + \left(C + \frac{h_{eq}}{\omega}\right)\frac{dy(\omega t)}{dt} + (k + k_{eq})y(\omega t) = BLi(\omega t) \tag{9}$$

$$k(X_0 - X_s) = F_{eq} \tag{10}$$

With the equivalent control equation of Eq. (8), the solution of the dynamic characteristics of the piston is thus transformed into solving a problem for the three equivalent coefficients of k_{eq}, h_{eq} and F_{eq}.

2.4. Solution for equivalent coefficients by describing function approach

The non-linear term in the control equation can be further analyzed using the describing function approach (Choe and Kim, 2000). The detailed process is given in Appendix A and the three equivalent

coefficients are determined as follows:

$$F_{eq}(\beta)=\frac{A_P P_l}{2\pi}\Big[\int_0^{\theta_2}\left(\frac{1+\beta}{1+\beta\cos\theta}\right)^n d(\theta)$$

$$+\alpha\int_{\pi}^{\theta_4}\left(\frac{1-\beta}{1+\beta\cos\theta}\right)^n d(\theta)$$

$$+\pi-\alpha\theta_2-\theta_4\Big] \tag{11}$$

$$k_{eq}(\beta)=\frac{2A_P P_l}{\pi S}\Big[\int_0^{\theta_2}\left(\frac{1+\beta}{1+\beta\cos\theta}\right)^n d(\sin\theta)$$

$$+\alpha\int_{\pi}^{\theta_4}\left(\frac{1-\beta}{1+\beta\cos\theta}\right)^n d(\sin\theta)$$

$$-(\alpha\sin\theta_2+\sin\theta_4)\Big] \tag{12}$$

$$h_{eq}=\frac{2A_P P_l}{\pi S}\left[\frac{n}{(n-1)\beta}(\alpha(\cos\theta_2+1)+\cos\theta_4-1)\right] \tag{13}$$

Thus, Eqs. (11) to (13) combined with Eq. (6) could determine an expression for the equivalent harmonic function of the gas forces in Fourier space. Using this expression, it is more efficient to evaluate the dynamic mechanical characteristic within the system of a DCLC during steady operation and can further investigate the coupling design between two compressors based on these properties.

3. The dynamic coupling model and design guidelines in multi-stage DCLC

3.1. The dynamic coupling model between two stages

Fig. 4 shows a schematic diagram of the coupling structure of a two-stage DCLC unit connected in series. The coupling characteristics mainly contain the following three aspects, namely:

(1) Pressure characteristics: The discharge pressure of the preceding compressor is the suction pressure of the following compressor, with the first stage pressure ratio $\alpha_1=P_1/P_0$ and the second one $\alpha_2=P_2/P_1$.
(2) Flow rate characteristics: According to the mass continuity law, the mass flow rate in the preceding stage must be the same as that in the following stage, but the volume flow rate of the preceding stage is significantly higher than that of the following one because of the change in average density of the medium.
(3) Boundary work characteristics: As the multi-stage DCLC unit is connected in series to obtain a higher pressure ratio, the boundary work of the preceding stage is not directly input to the JTC unit, but first to the following stage instead.

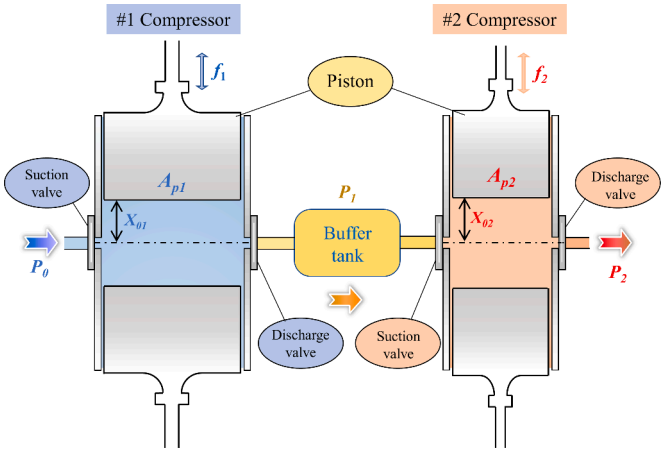

Fig. 4. Schematic diagram of the coupling structure between two stages.

Fig. 5 shows the pressure waveforms before and after the buffer tank which are measured by a pressure sensor and a manometer, respectively. The flow provided by a linear compressor shows a gas pulsation effect caused by the suction and discharge valves. A direct connection between two linear compressors might result in a severe vibration abnormality, especially when the two compressors operate at the same frequency. The buffer tank between each two stages has the effect of smoothing the waveform and transforming the pulse waveform from the preceding compressor into a smooth waveform. The gas in the buffer tank is a turbulent flow with a computable flow resistance, which can be determined as (Bell et al, 2020):

$$\Delta P=K_r\frac{G^2}{2\rho D_b^4} \tag{14}$$

where G is the mass flow rate of the medium, D_b is the equivalent diameter and K_r is the local resistance factor, which is an experimental measurement value. For the buffer tank used in the authors' laboratory, the local resistance factor is approximated according to the flow rates as:

$$K_r=\frac{7.598E5}{Re} \tag{15}$$

where Re is the Reynolds number of the fluid in the buffer tank.

3.2. Control volume

Creating a control volume among the connecting line and buffer tank between the two stages is the basis for investigating the coupling principles between two stages. Fig. 6 shows a schematic of control volume and its main transfer terms. The following simplifying assumptions are made for this control volume (Bell et al, 2020):

(1) The flow resistance of the buffer tank is much less than the absolute pressure in its operating condition ($\Delta P<<P$), the entire control volume has a uniform pressure value.
(2) The entire control body has a uniform temperature value and the temperature is the same as the ambient temperature.

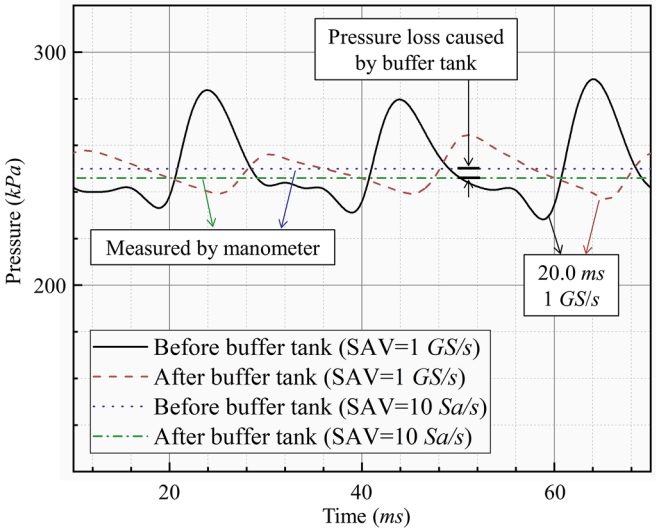

Fig. 5. Pressure wave measured in the buffer tank.

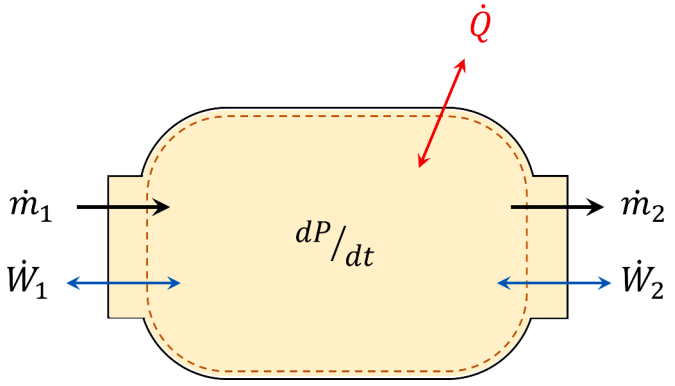

Fig. 6. Control volume between two stages of the compressor.

(3) The heat transfer between the medium in the control volume and that outside is only achieved by the heat convection by the walls.
(4) Ignore the change in kinetic energy of the gas in the control volume.
(5) Ignore the gravitational effect of the gas.

For this control volume using He-4 as the work medium, the thermodynamic state of the entire control volume can be determined by only one strength parameter which is the pressure based on the assumptions (1) to (5).

The control volume system is a steady-state one, and in a period of time, according to the mass continuity law, we have:

$$\frac{\Delta m}{\Delta t} = \int \dot{m}_1 + \int \dot{m}_2 = 0 \tag{16}$$

where $\dot{m}_1$ is the mass flow rate from the preceding stage into the control volume and $\dot{m}_2$ is the mass flow rate from the control volume to the following stage. According to the ideal *P-V* curve in Fig. 3, and combine with Eqs. (5) and (A10) we have:

$$f_1 A_{P1} \frac{P_{cv}}{RT_{cv}} \left(x_{1,3} - x_{1,2}\right) + f_2 A_{P2} \frac{P_{cv}}{RT_{cv}} \left(x_{2,1} - x_{2,4}\right) = 0 \tag{17}$$

where f_1 and f_2 are the operating frequencies of the preceding and following stages, respectively, and A_{p1} and A_{p2} are the cross-sectional area of the piston in the preceding and following stages. The conservation of energy equation for the control volume is then expressed as:

$$\frac{\Delta U}{\Delta t} = \dot{Q} + \dot{W}_1 - \dot{W}_2 + \dot{m}_1 h_1 - \dot{m}_2 h_2 \tag{18}$$

where $\dot{Q}$ is the heat exchange between the control volume and the environment through the walls and $\dot{W}_1$ is the boundary work term inputted to the control body from the preceding stage. Ideally, for a DCLC according to Fig. 3 and combine with Eq. (5) we have:

$$\dot{W}_1 = -f_1 P_{cv} A_{p1} \cdot \left(x_{1,3} - x_{1,2}\right) \tag{19}$$

Similarly, $\dot{W}_2$ is the boundary work of the control volume inputted to the following compressor and according to Eq. (5):

$$\dot{W}_2 = -f_2 P_{cv} A_{p2} \cdot \left(x_{2,1} - x_{2,4}\right) \tag{20}$$

For the control volume consisting of a buffer tank, the relationship h_1=h_2 exists because the pressure and temperature of the medium remain unchanged.

3.3. Design guidelines and considerations

For a multi-stage DCLC unit in series we can use a pressure ratio loss (PRL) to evaluate the coupling performance, taking a two-stage compressor system as an example, which is defined as:

$$PRL = 1 - \frac{\alpha_{1,2}}{\alpha_1 \cdot \alpha_2} \tag{21}$$

where α_1 and α_2 are the maximum pressure ratio of the first and second compressors, respectively, and $\alpha_{1,2}$ is the maximum pressure ratio of the coupling compressors.

In order to obtain the optimum coupling performance, the design principle is as follows: when both stages of compressors are operating at full stroke, they need to have exactly the same delivery characteristics, which are also the same as the one when these compressors are operating individually. It indicates that when the two compressors with perfect coupling parameters are operating separately at full stroke, the boundary work delivered from the preceding stage to the control volume described in the previous chapter can exactly match the one delivered from the control volume to the following stage, at which time the heat exchange between the control volume and the environment is zero, the enthalpy of the gas in the control volume remains unchanged.

From this coupling principle, the following relationships exist between the preceding and following stages:

$$f_1 A_{P1} P_1 \left(x_{1,2} - x_{1,3}\right) = f_2 A_{P2} P_1 \left(x_{2,1} - x_{2,4}\right) \tag{22}$$

The boundary work delivered to the control volume by the preceding stage can also be expressed as the mechanical work done by the gas force on the medium during the piston discharge phase (phase θ_2 to θ_3), using the equivalent non-linear dynamic model we have:

$$\left| \int_{X_0+\frac{S_1}{2}\cos\theta_2}^{X_0+\frac{S_1}{2}\cos\theta_3} f_{g,eq,1}(x)dx \right| = \left| \int_{X_0+\frac{S_2}{2}\cos\theta_4}^{X_0+\frac{S_2}{2}\cos\theta_1} f_{g,eq,2}(x)dx \right| \tag{23}$$

where

$$f_{g,eq}(\theta) = k_{eq} s(\omega t) - \frac{h_{eq}}{\omega} s(\dot{\omega} t) + F_{eq}$$

To simplify this expression, by substituting Eq. (A10) into Eq. (19), the boundary work delivered from the preceding stage to the control volume can be expressed as:

$$W_1 = \frac{\pi f_1 d_1^2 P_1}{4} \left(\left(\frac{P_1}{P_0}\right)^{-\frac{1}{n}} \left(X_{0,1} + \frac{S_1}{2}\right) - \left(X_{0,1} - \frac{S_2}{2}\right) \right) \tag{24}$$

Similarly, the boundary work delivered from the control volume to the following stage can be obtained by substituting Eq. (A10) into Eq. (20), which is:

$$W_2 = \frac{\pi f_2 d_2^2 P_1}{4} \left(\left(X_{0,2} + \frac{S_2}{2}\right) - \left(\frac{P_2}{P_1}\right)^{\frac{1}{n}} \left(X_{0,2} - \frac{S_2}{2}\right) \right) \tag{25}$$

It follows that, for an ideal compression and expansion cycle of an ideal gas, the lowest pressure ratio loss is achieved when the two compressors satisfy the following relationship:

$$f_1 d_1^2 \left(\left(\frac{P_1}{P_0}\right)^{-\frac{1}{n}} \left(X_{0,1} + \frac{S_1}{2}\right) - \left(X_{0,1} - \frac{S_2}{2}\right) \right) = f_2 d_2^2 \left(\left(X_{0,2} + \frac{S_2}{2}\right) - \left(\frac{P_2}{P_1}\right)^{\frac{1}{n}} \left(X_{0,2} - \frac{S_2}{2}\right) \right) \tag{26}$$

where $X_{0,1}$ and $X_{0,2}$ represent the dynamic equilibrium positions of the preceding and following stages of compressors, respectively, and S_1 and S_2 represent the maximum piston strokes of the two stages of compressors, respectively.

In addition, considering the mass continuity of a two-stage compressor system in series, there is:

$$f_1 A_{P1}\rho_0\left(x_{1,1}-x_{1,4}\right)=f_1 A_{P1}\rho_1\left(x_{1,2}-x_{1,3}\right)$$

$$=f_2 A_{P1}\rho_1\left(x_{2,1}-x_{2,4}\right)=f_2 A_{P2}\rho_2\left(x_{2,2}-x_{2,3}\right) \quad (27)$$

Comparing Eq. (22) with Eq. (27), it is found that for ideal gases satisfying the Clausius–Clapeyron relation, two compressors satisfying the mass continuity law must deliver the same boundary work in accordance with Eq. (40). For non-ideal gases the principle requires to adjust the structural design parameters to converge to Eq. (40) in order to obtain the optimum coupling performance. Fig. 7 shows the *P-V* curve for a two-stage DCLC unit in an ideal compression expansion cycle satisfying the optimal coupling parameters, where the area of the shadow region represents the boundary work transported between the control volume and two compressors.

3.4. Design process and parameter correction

Through the above analysis, the design of the two-stage DCLC unit includes the determination of three types of parameters. The first are the suction and discharge pressures of the two compressors. The second are the structural parameters of the cylinder. The third are the operating parameters of the compressors. At the beginning of the design, determining the suction and discharge pressures of each stage is of great significant. The actual demand and the maximum pressure ratio of each stage should be considered for subsequent coupling design. To determine the initial pressure, the ultimate pressure ratio of the DCLC should be obtained. The ultimate pressure ratio of a single-stage moving-coil DCLC is affected by the ratio of sweeping volume to dead volume, the operating frequency, the charge pressure and other minor factors. Fig. 8 shows the experimental pressure ratio for the DCLCs with different piston diameters developed in the authors' laboratory. For the diameter, or more precisely, for the sweeping volume, a larger value means a higher pressure ratio within a certain range without the blocked flow. And for the charge pressure, it shows that the pressure ratio first rises and then decreases with it.

The number of stages to be connected can be determined from the pressure ratio of each compressor and the total suction pressure required by the system. Once the number of stages has been determined, the suction and discharge pressures of each stage need to be determined based on the maximum performance of the single-stage DCLC tested in Fig. 8, and the initial pressure required is estimated using Eq. (28):

$$P_{charge}=\frac{P_{discharge}+P_{suction}}{2} \quad (28)$$

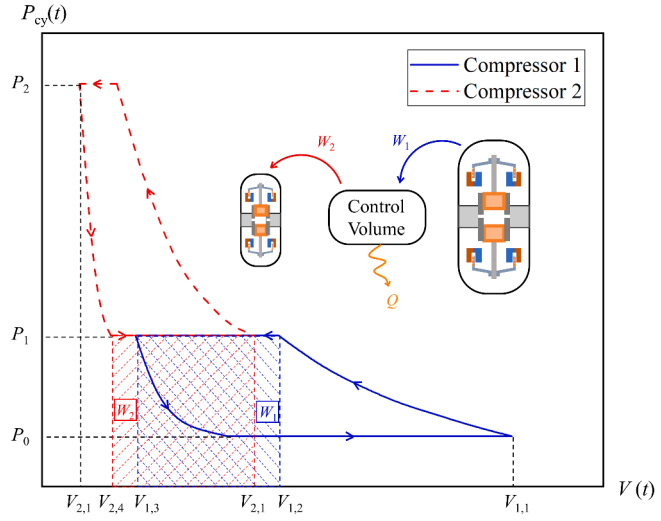

Fig. 7. *P-V* curve of the two-stage DCLC unit.

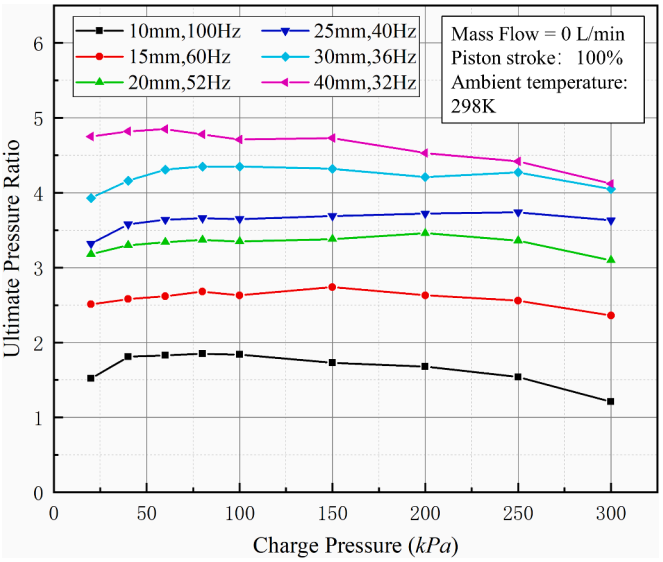

Fig. 8. Relationship between the ultimate pressure ratio and the charge pressure.

Also taking a two-stage DCLC unit in series as an example, the pressure P_0, P_1, P_2 are determined firstly and need to satisfy Eq. (29):

$$\alpha_1=P_1/P_0\le\alpha_{max}\ \text{when}\ P_{charge}=\frac{P_0+P_1}{2} \quad (29)$$

$$\alpha_2=P_2/P_1\le\alpha_{max}\ \text{when}\ P_{charge}=\frac{P_1+P_2}{2}$$

By the determined suction and discharge pressure, the structural parameters of the cylinder can be further determined. In the design process, it is of great significance that each stage of DCLC have the same stroke in order to simplify the overall design of a multi-stage DCLC unit, so here the stroke is regarded as a fixed value and then the piston diameter for each stage can be determined.

Taking P_0, P_1, P_2, and the fixed X_0 and S into Eq. (26), the following relationship can be obtained between the piston diameters of the preceding and following stages:

$$f_1 d_1^2=k f_2 d_2^2 \quad (30)$$

where

$$k=\left[\left(X_0+\frac{S}{2}\right)-\left(\frac{P_2}{P_1}\right)^{\frac{1}{n}}\left(X_0-\frac{S}{2}\right)\right]\Big/\left[\left(\frac{P_1}{P_0}\right)^{-\frac{1}{n}}\left(X_0+\frac{S}{2}\right)-\left(X_0-\frac{S}{2}\right)\right]$$

By Eq. (30) it has been determined that the coupling relationship between the piston diameters of the two stages, and finally a reasonable operating frequency need to be selected to complete the overall design. There is a resonant frequency for any DCLC, the resonant frequency is determined as (Marquardt et al, 1992):

$$f=\frac{1}{2\pi}\sqrt{\frac{k_g+k_s}{m}} \quad (31)$$

where k_s is the stiffness of the flexure springs and k_g is the stiffness of the gas spring, which is determined by Eq. (12).

Now the design of the coupling structure of the two-stage DCLC unit under the ideal compression expansion model is finished. After the structural parameters of the cylinder are determined, the design of the other parameters, including the magnet structure, moving-coil structure and etc. can be acquired (Marquardt et al, 1992).

It is noted that the above designs are all based on the ideal model shown in Fig. 3, while for the actual cycle there are four factors to be considered:

(1) The compression (expansion) process of the actual cycle is not an ideal isentropic process, and this non-ideal characteristic can be corrected by adjusting the exponential coefficient.
(2) There is no clear boundary line between the compression and discharge processes in the actual cycle, which makes the phase angle θ_2 and θ_4 cannot be calculated accurately.
(3) The suction and discharge valves of the DCLC are reed valves, which have a certain delay time during operating.
(4) The piston offset will occur during the operation of the DCLC at high pressure ratios (Liang, 2018), and the piston offset is particularly significant for the compressor operating in low charge pressure (Zhao et al, 2022), so the additional correction is required for the compressor with low operating pressure.

The non-ideal considerations, combined with practical experience, lead to a correction factor for the piston diameter of each stage based on the average operating pressure as shown in Table 1.

According to the above analyses, the design flow chart for designing a four-stage DCLC unit with high pressure ratio is suggested in Fig. 9, which aims to ensure that the four compressors to obtain the optimal coupling performance.

4. Experiment verifications in a hybrid cryocooler operating in 1–2 K using a four-stage DCLC unit

For a hybrid cryocooler operating in 1–2 K, the suction pressure after the throttling valve needs to be lower than 3.1 kPa, while the pressure before the throttling valve needs to reach 160 kPa at least to ensure that the cooling power generated by the throttling process is sufficient to balance the heat radiation (Dang et al, 2022). The designed high pressure of 200 kPa as well as the designed low pressure of 1.7 kPa are preliminarily drawn up to satisfy the requirement of the hybrid cryocooler. According to the design process in Section 3.4, the structural parameters and some operating parameters are determined as shown in Table 2.

The maximum pressure ratios of the four stages are mainly determined by the structural parameters such as the piston diameters and the compressor strokes. They are affected by the charge pressure in the test about the single-stage. Thus, based on the coupling model, the initial values of the pressures between each stage should be firstly given, and then the structural parameters are determined. And then the maximum pressure ratios of each stage can be determined by the experimental results in Fig. 8. In another word, the maximum pressure ratios in Table 2 are preliminarily calculated by the structural parameters and finally determined by the experimental results in a standalone test platform.

4.1. Standalone compressor tests

After determining the structural dimensions of each compressor, a standalone test platform at ambient temperature is developed as shown in Fig. 10, pressure sensors are provided before and after each stage to monitor the pressure.

The four-stage DCLC unit uses a needle valve as the simulated load in the close cycle. Each stage has a separate AC power to supply input voltage with design frequency. The test ambient temperature is 300 K

Table 1
Scale factors of actual compression and expansion cycle.

Average charge pressure (kPa)	Scale factors
< 20	1.16–1.25
20–80	1.05–1.09
80–300	1.02–1.05
300–1000	0.98–1.02
> 1000	0.90–0.98

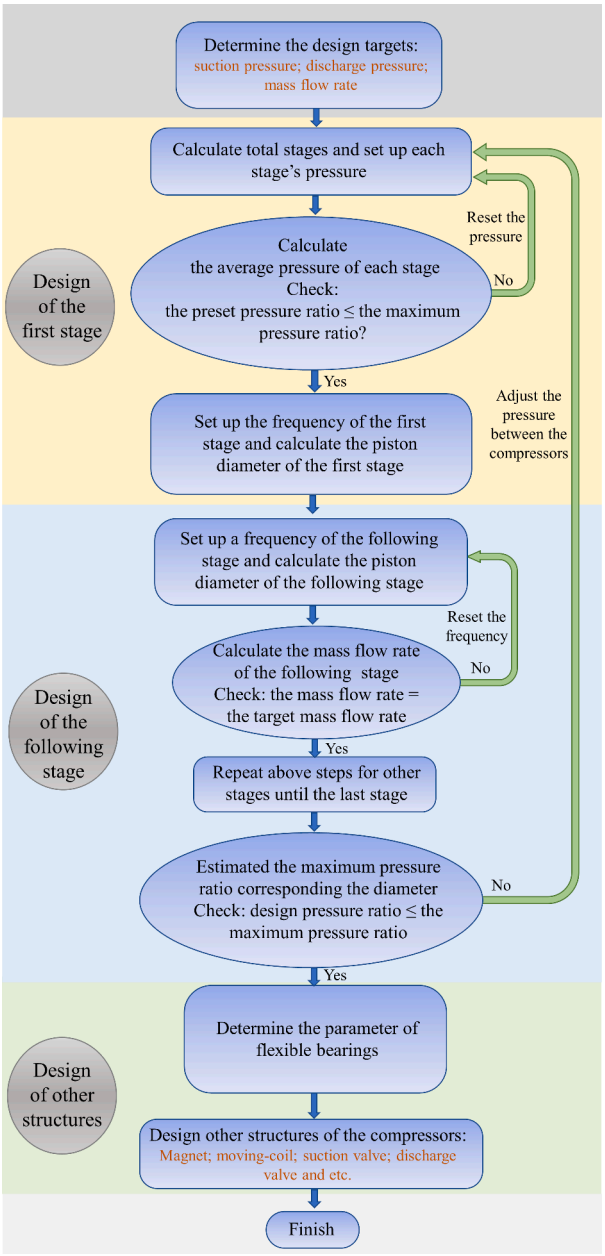

Fig. 9. Design flow chart of four-stage DCLC to achieve the optimum coupling performance.

Table 2
The structural parameters and operating parameters of the four-stage DCLC unit.

Parameters	Values
Designed high pressure	200 kPa
Designed low pressure	1.70 kPa
Compressor stroke	11.0 mm*2 (Dual-opposed)
Operating frequency	f_1=30 Hz, f_2=40 Hz, f_3=60 Hz, f_4=98 Hz
Piston diameters	d_1=45.1 mm, d_2=25.4 mm, d_3=15.2 mm, d_4=11.3 mm
Maximum pressure ratio (single-stage)	α_1=5.3, α_2=4.2, α_3=2.8, α_4=1.9,
Compressor mass	m_1=6.8 kg, m_2=6.5 kg, m_3=6.3 kg, m_4=2.8 kg
Compressor sizes	φ120 mm*280 mm(1st 2nd 3rd), φ80*130 mm (4th)

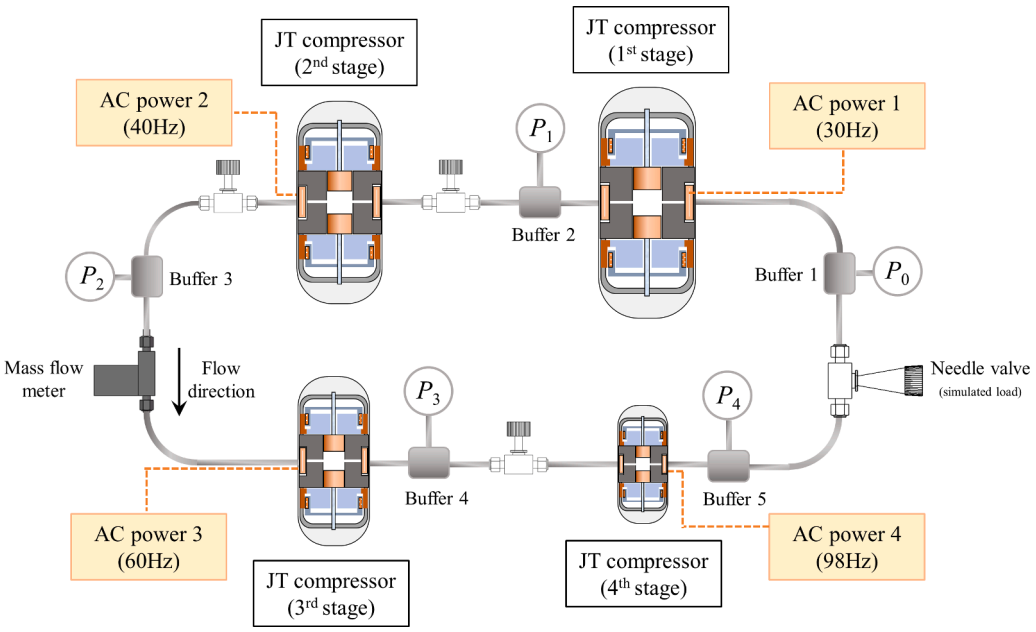

Fig. 10. Standalone test platform of the four-stage DCLC unit.

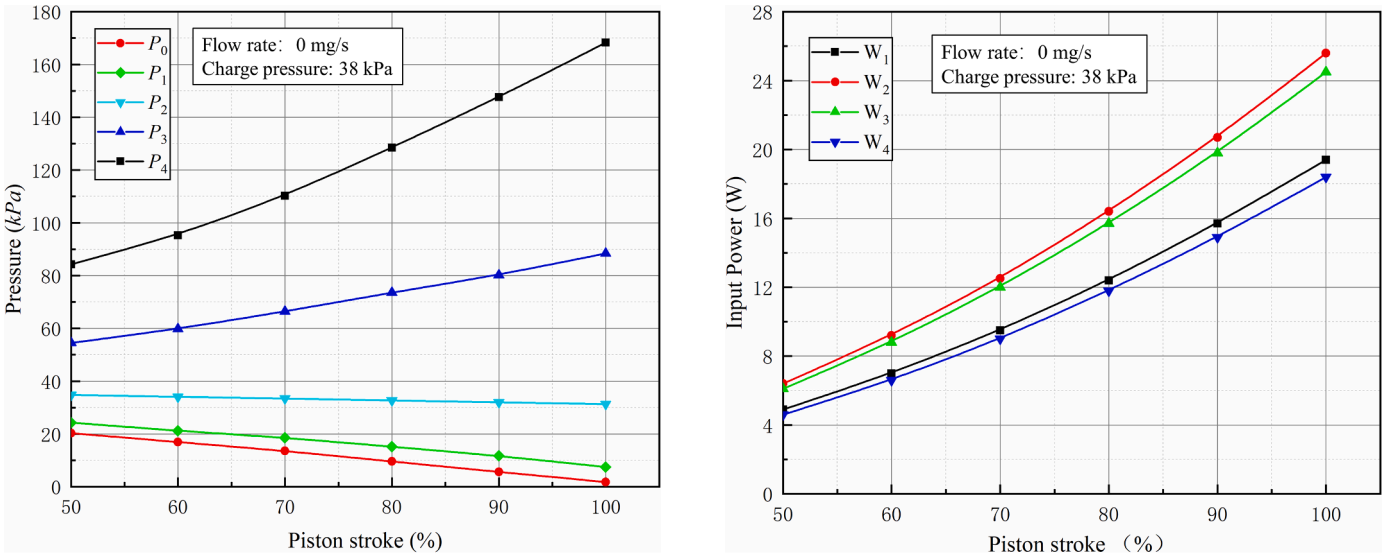

Fig. 11. Relationship between the piston stroke and (a) the pressure of each stage (b) the input power of each compressor.

and the charge pressure is 38 kPa.

Fig. 11(a) shows the change of pressure in each stage as a function of the input power with no flow rate. The suction pressure of the first stage compressor decreases to 2.1 kPa when the stroke reaches its maximum value, meanwhile, the discharge pressure of the fourth stage compressor comes to 215.3 kPa, with a total pressure ratio (TPR) of 102.5, giving a PRL of 13.4%.

Fig. 11(b) shows the change in the input power of each stage as the stroke increases, with 19.4 W, 25.6 W, 24.5 W and 18.4 W for the four compressors at its maximum stroke, respectively. Moreover, it is found that the input power and the boundary work estimated by Eq. (32) are similar for the four compressors. The boundary work of each stage is 14.7 W, 17.8 W, 16.9 W and 14.1 W, respectively.

$$W_{PV} \approx W_{input} - \frac{1}{2}i^2R \tag{32}$$

The similarity of boundary work is consistent with the theoretical analyses and proves that the coupling characteristics of the four compressors in series are reasonable.

The verification of the design principle is shown in Fig. 12 which shows a good agreement between the modeling and experimental results. The pressure in Fig. 12 is obtained when the piston operates at full stroke. It can be observed that the experimental pressure ratios of the first through the third stages are all slightly lower than the corresponding simulated ones in the model, and the differences are caused by the following factors. First, the average experimental pressures in the first through the third stages are all much lower than the corresponding simulated ones which causes an unexpected malfunction in the valve modules. Second, the piston diameters of the preceding three stages are larger than that of the last stage, and thus the influence of the gas spring force, which is ignored in the dynamic model, becomes obvious.

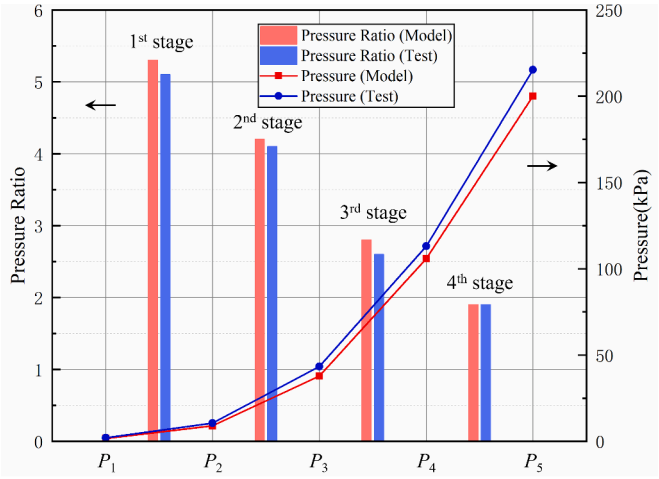

Fig. 12. Comparisons of the modelling and experimental results.

Furthermore, it is observed that during the experiments, there is almost no heat dissipation from the interstage buffer tank, which further proves that few loss is generated between stages.

4.2. Performance tests in the hybrid compressor

After the DCLC unit has been tested independently in the standalone test platform, it is also coupled with the JTC in the hybrid cryocooler as a drive source, providing the required suction and high pressures for the JTC. The schematic diagram of structure of the hybrid cryocooler is shown in Fig. 13, which consists of a JTC with a four-stage thermal coupled SPTC as the pre-cooling stage. The main parameters of the four-stage SPTC is shown in Table 3 (Dang et al, 2020). The thermal coupling platform of pre-cooling stage is respectively set at 80 K, 40 K and 10 K to provide cooling capacity for the medium in the JT refrigeration cycle through the pre-cooling heat exchanger. The four-stage DCLC unit is located outside the vacuum chamber at ambient temperature. The four stages of counter-flow heat exchanger between the JT throttle valve and the ambient temperature ensure that the majority of the cooling capacity is kept in the vacuum chamber.

The cooling down curves for each stage are shown in fig. 14(a). The entire cool down lasts about eighteen hours. During the process, the precooling PTCs are cooled down to the aimed temperatures quickly and the final stable temperature of the three precooling heat exchangers are

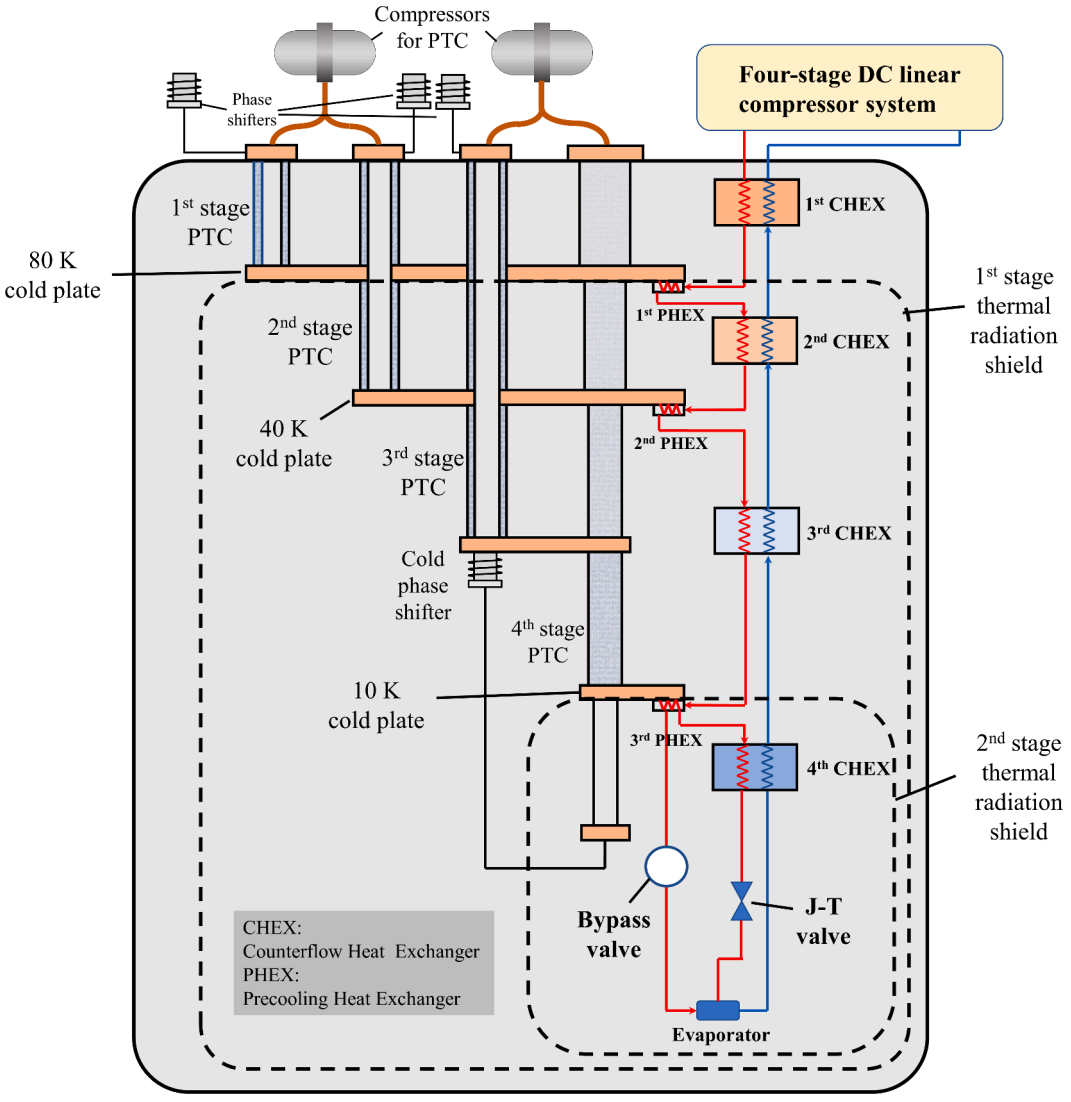

Fig. 13. Schematic of the system structure of the hybrid cryocooler.

Table 3
Main parameters of each stage component of the four-stage SPTC.

	1st stage	2nd stage	3rd stage	4th stage
Regenerator (mm)	Φ24×64	I: Φ20×40 II: Φ20×30	I: Φ16×45 II: Φ16×40 III: Φ16×38	I: Φ14×36.4 II: Φ12×28.2 III: Φ12×31.2 IV: Φ10×36
Pulse tube (mm)	Φ14×76	Φ12×81	Φ9×128	Φ8×80
Inertance tube (mm)	I: Φ3.5×2800 II: Φ4.5×1400	I: Φ3×3200 II: Φ4.5×1200	I: Φ3×800 II: Φ4×1180	I: Φ3×320 II: Φ4×1260
Gas reservoir (mm)	Φ60×80	Φ60×80	Φ30×65	Φ30×55
Frequency (Hz)	55.0	55.0	30.5	30.5
Average pressure (MPa)	3.3	3.3	1.2	1.2

72 K, 41 K and 8.9 K, respectively. At the thirteenth hour, the bypass valve is closed and the JT throttling valve begins to work. In the end the temperature of the evaporator reaches 1.8 K.

Fig. 14(b) shows the detailed cooling curve of the evaporator from the twelfth hour to the twentieth hour of the cooling process and the changes of corresponding pressure and mass flow rate. After the system is operating stably over about 17 hours, the pressure before the throttling valve is finally maintained at 178 kPa and the pressure after the one is reduced to 1.75 kPa, slightly higher than the design pressure, at which point, with the PRL of 14.1%, the TPR reaches 101.7. By comparison, a conventional single-stage moving-coil type DCLC can only achieve a typical pressure ratio of lessen than 5. Therefore, it is a significant approach of greatly enhancing the pressure ratio of the moving-coil type DCLC by series connection. Fig. 15 shows the relationship between the pressure at each stage and stroke during stable process.

It should be noted that the reason for the much higher charge pressure in the actual JT refrigeration cycle than in the standalone test is that a large amount of medium will transform into non-gas phase at low temperature under 4.2 K. Furthermore, it is also worth noting that the mass flow rate of these two experiments is slightly different which is caused by the different densities of the helium flowing through the load. The volumetric flow rate is close for the two experiments. However, the density of the helium flowing through the JT throttling valve is larger than that of the simulated load in the ambient temperature test.

5. Conclusions

As a key component of the JTC operating in 1–2 K, the four-stage DCLC unit is required to provide an extremely low suction pressure of below 3.1 kPa for the throttle process. In this paper, an equivalent nonlinear dynamic model is proposed to analyze the gas spring force within the cylinder. Based on the model, the coupling principle among stages is analyzed to obtain the optimal coupling characteristics.

The analyses of the coupling principle show that there are three types of parameters which affect the coupling characteristics between each two stages, namely, the preset pressure parameters, the structural parameters of the cylinder, and the operating parameters. A novel design method of the structural parameters and operating frequency are analyzed, so that the four-stage DCLC unit can obtain the optimal coupling characteristics.

A standalone test platform for the four-stage DCLC unit is designed to verify the design method. The experimental results show that the four-stage DCLC unit with the designed parameters achieves a suction pressure of 2.1 kPa, with a TPR of 102.5 and a PRL of 13.4%. Furthermore, the four-stage DCLC unit is tested in an actual hybrid cryocooler

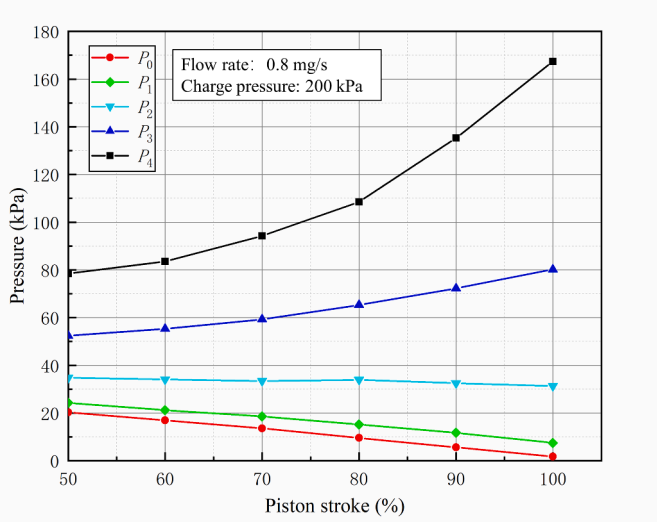

Fig. 15. Relationship between the piston stroke and the pressure of each stage.

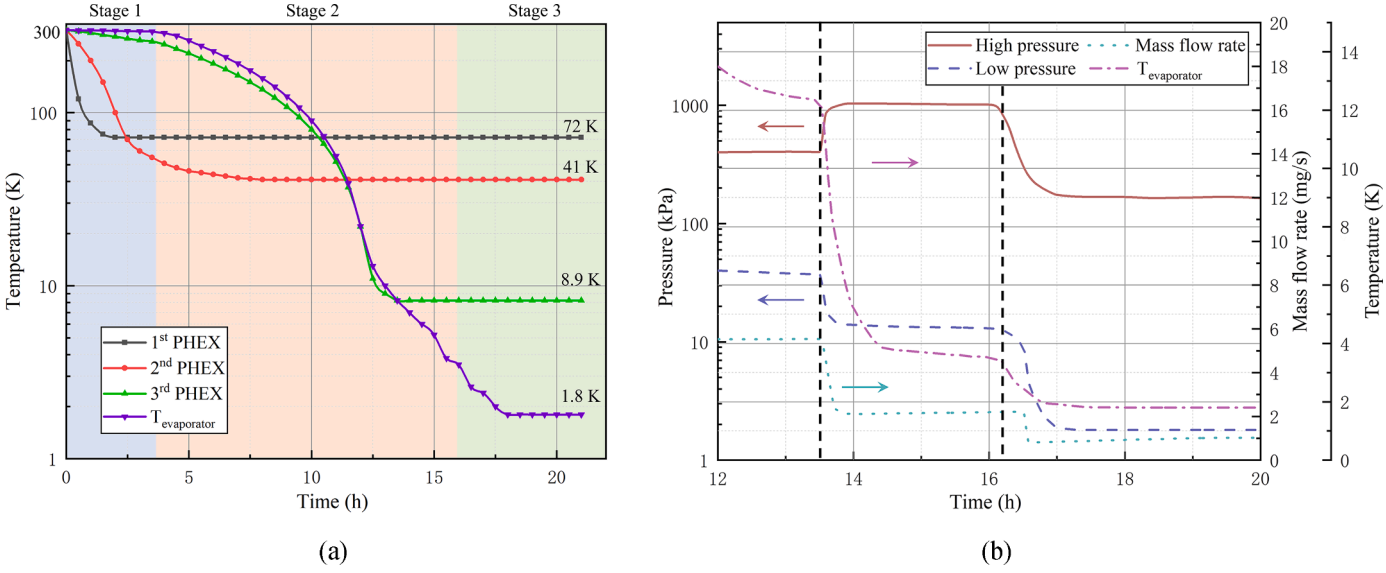

Fig. 14. Cooling down curves of (a)the hybrid cryocooler (b)the details for the evaporator from the twelfth hour to the twentieth hour.

consisted of a four-stage SPTC and a JTC, and acquires a suction pressure of 1.75 kPa, with a TPR of 101.7 and a PRL of 14.1%, which makes it feasible for the hybrid cryocooler to successfully achieve 1.8 K. The general consistency between the designed values and experimental results is observed and the rationality and feasibility of the coupling principle are experimentally verified.

Declaration of Competing Interest

The authors declare that they have no known competing financial interests or personal relationships that could have appeared to influence the work reported in this paper.

Acknowledgements

This work is supported by the National Natural Science Foundation of China (Grant No. 52076210), Shanghai Municipal Science and Technology Major Project (Grant No. 2019SHZDZX01) and Major Project of Science and Technology Commission of Shanghai Municipality (Grant No. 22511100100). The authors also greatly appreciate other supports from Shanghai Municipality (Grant Nos. 2019-jmrh2-kj2 and 2021-cyxt2-kj09).

Appendix A

The derivation process of Eqs. (11) through (13) is shown as follows:

For the gas force in Eq. (5), which is a periodic function in non-harmonic form with a period of 2π, the Fourier expansion function is:

$$f_g(t) = \frac{A_0}{2} + \sum_{n=1}^{\infty}(A_n \cos n\omega t + B_n \sin n\omega t) \tag{A1}$$

$$A_0 = \frac{1}{\pi}\int_0^{2\pi} f_g(t)d(\omega t) \tag{A2}$$

$$A_n = \frac{1}{\pi}\int_0^{2\pi} f_g(t)\cos n\omega t d(\omega t) \tag{A3}$$

$$B_n = \frac{1}{\pi}\int_0^{2\pi} f_g(\omega t)\sin n\omega t d(\omega t) \tag{A4}$$

Taking the second level of the describing function of $f_g(t)$ as:

$$\widetilde{f_g(t)} = \frac{A_0}{2} + A_1\cos\omega t + B_1\sin\omega t \tag{A5}$$

where:

$$\begin{aligned} A_0 &= \frac{1}{\pi}\int_0^{2\pi} f_g(\omega t)d(\omega t) \\ &= \frac{A_P P_l}{\pi}\int_0^{\theta_2}\left(\frac{X_0 + S/2}{X_0 + S\cos\omega t/2}\right)^n d(\omega t) \\ &+ \frac{A_P P_h}{\pi}\int_{\theta_2}^{\pi} d(\omega t) \\ &+ \frac{A_P P_h}{\pi}\int_{\pi}^{\theta_4}\left(\frac{X_0 - S/2}{X_0 + S\cos\omega t/2}\right)^n d(\omega t) \\ &+ \frac{A_P P_l}{\pi}\int_{\theta_4}^{2\pi} d(\omega t) \end{aligned} \tag{A6}$$

$$\begin{aligned} A_1 &= \frac{1}{\pi}\int_0^{2\pi} f_g(\omega t)\cos\omega t d(\omega t) \\ &= \frac{A_P P_l}{\pi}\int_0^{\theta_2}\left(\frac{X_0 + S/2}{X_0 + S\cos\omega t/2}\right)^n \cos\omega t d(\omega t) \end{aligned}$$

$$+\frac{A_P P_h}{\pi}\int_{\theta_2}^{\pi}\cos\omega t d(\omega t)$$

$$+\frac{A_P P_h}{\pi}\int_{\pi}^{\theta_4}\left(\frac{X_0 - S/2}{X_0 + S\cos\omega t/2}\right)^n \cos\omega t d(\omega t)$$

$$+\frac{A_P P_l}{\pi}\int_{\theta_4}^{2\pi}\cos\omega t d(\omega t) \tag{A7}$$

$$B_1 = \frac{1}{\pi}\int_0^{2\pi} f_g(\omega t)\sin\omega t d(\omega t)$$

$$=\frac{A_P P_l}{\pi}\int_0^{\theta_2}\left(\frac{X_0 + S/2}{X_0 + S\cos\omega t/2}\right)^n \sin\omega t d(\omega t)$$

$$+\frac{A_P P_h}{\pi}\int_{\theta_2}^{\pi}\sin\omega t d(\omega t)$$

$$+\frac{A_P P_h}{\pi}\int_{\pi}^{\theta_4}\left(\frac{X_0 - S/2}{X_0 + S\cos\omega t/2}\right)^n \sin\omega t d(\omega t)$$

$$+\frac{A_P P_l}{\pi}\int_{\theta_4}^{2\pi}\sin\omega t d(\omega t) \tag{A8}$$

where θ_2 and θ_4 are the phase angles at the position of point 2 and point 4 in the *P-V* curve of the cylinder in Fig. 3, respectively, which are the transition phase points in the cylinder from an adiabatic process to an isobaric process. θ_2 and θ_4 are determined by the suction and discharge pressures:

$$\begin{cases}\theta_2 = \pi \\ \theta_4 = 2\pi\end{cases} \text{ for } \frac{S}{2X_0} \le \varepsilon \tag{A9}$$

$$\begin{cases}\theta_2 = arccos\left[\dfrac{2X_0}{S}\left(\alpha^{-\frac{1}{n}}\left(1+\dfrac{S}{2X_0}\right)-1\right)\right] \\ \theta_4 = arccos\left[\dfrac{2X_0}{S}\left(\alpha^{\frac{1}{n}}\left(1-\dfrac{S}{2X_0}\right)-1\right)\right]\end{cases} \text{ for } \frac{S}{2X_0} > \varepsilon \tag{A10}$$

where $\alpha = P_h/P_l$, is the actual pressure ratio of the compressor, and ε is defined as:

$$\varepsilon = \frac{\alpha^{\frac{1}{n}} - 1}{\alpha^{\frac{1}{n}} + 1} \tag{A11}$$

So far, by integrating the results of Eqs. (A6) (A7) and (A8), the coefficients A_0, A_1, B_1 of the describing function can be obtained as a function of the stroke S and the center position X_0 of the piston, and by comparing the equivalent gas force of Eq. (6) with the describing function of Eq. (A5) it can be obtained as follows:

$$F_{eq} = \frac{A_0(X_0, S)}{2} - \frac{A_p(P_h + P_l)}{2} = \frac{1}{2\pi}\int_0^{2\pi} f_g(\omega t)d(\omega t) - \frac{A_p(P_h + P_l)}{2} \tag{A12}$$

$$k_{eq} = \frac{2A_1(X_0, S)}{S} = \frac{2}{\pi S}\int_0^{2\pi} f_g(\omega t)\cos\omega t d(\omega t) \tag{A13}$$

$$h_{eq} = \frac{2B_1(X_0, S)}{S} = \frac{2}{\pi S}\int_0^{2\pi} f_g(\omega t)\sin\omega t d(\omega t) \tag{A14}$$

The three equivalent coefficients F_{eq}, k_{eq} and h_{eq} in the equivalent gas force $f_{eq}(t)$ can thus be replaced by the describing function approach in terms of the dynamic equilibrium position X_0 and the stroke S. The dynamic equilibrium position X_0 is an uncertain parameter and thus needs to be defined according to Eq. (10) as:

$$X_0 = X_s + \frac{F_{eq}}{k} \tag{A15}$$

Then letting $\beta = S/(2X_0)$ and substituting it into Eqs. (A12) to (A14) to obtain the dimensionless equivalent elasticity coefficient k_{eq}, equivalent viscosity coefficient h_{eq}, and equivalent static force F_{eq} as:

$$\begin{aligned} F_{eq} &= \frac{1}{2\pi}\int_0^{2\pi} f_g(\theta)d(\theta) \\ &= \frac{A_P P_l}{2\pi}\Big[\int_0^{\theta_2}\left(\frac{1+\beta}{1+\beta\cos\theta}\right)^n d(\theta) + \alpha\int_{\theta_2}^{\pi} d(\theta) \\ &+\alpha\int_{\pi}^{\theta_4}\left(\frac{1-\beta}{1+\beta\cos\theta}\right)^n d(\theta) \\ &+\int_{\theta_4}^{2\pi} d(\theta) - \pi(\alpha+1)\Big] \end{aligned} \tag{A16}$$

$$\begin{aligned} k_{eq} &= \frac{2}{\pi S}\int_0^{2\pi} f_g(\theta)\cos\theta d(\theta) \\ &= \frac{2A_P P_l}{\pi S}\Big[\int_0^{\theta_2}\left(\frac{1+\beta}{1+\beta\cos\theta}\right)^n \cos\theta d(\theta) \\ &+\alpha\int_{\theta_2}^{\pi}\cos\theta d(\theta) \\ &+\alpha\int_{\pi}^{\theta_4}\left(\frac{1-\beta}{1+\beta\cos\theta}\right)^n \cos\theta d(\theta) \\ &+\int_{\theta_4}^{2\pi}\cos\theta d(\theta) \end{aligned} \tag{A17}$$

$$\begin{aligned} h_{eq} &= \frac{2}{\pi S}\int_0^{2\pi} f_g(\theta)\sin\theta d(\theta) \\ &= \frac{2A_P P_l}{\pi S}\Big[\int_0^{\theta_2}\left(\frac{1+\beta}{1+\beta\cos\theta}\right)^n \sin\theta d(\theta) \\ &+\alpha\int_{\theta_2}^{\pi}\sin\theta d(\theta) \\ &+\alpha\int_{\pi}^{\theta_4}\left(\frac{1-\beta}{1+\beta\cos\theta}\right)^n \sin\theta d(\theta) \\ &+\int_{\theta_4}^{2\pi}\sin\theta d(\theta)\Big] \end{aligned} \tag{A18}$$

Rewrite and simplify Eqs. (A16) to (A18) as:

$$\begin{aligned} F_{eq}(\beta) = \frac{A_p P_l}{2\pi}\Big[&\int_0^{\theta_2}\left(\frac{1+\beta}{1+\beta\cos\theta}\right)^n d(\theta) \\ &+\alpha\int_{\pi}^{\theta_4}\left(\frac{1-\beta}{1+\beta\cos\theta}\right)^n d(\theta) \end{aligned}$$

$$+\pi-\alpha\theta_2-\theta_4] \tag{11}$$

$$k_{eq}(\beta)=\frac{2A_P P_l}{\pi S}\left[\int_0^{\theta_2}\left(\frac{1+\beta}{1+\beta\cos\theta}\right)^n d(\sin\theta)\right.$$

$$+\alpha\int_{\pi}^{\theta_4}\left(\frac{1-\beta}{1+\beta\cos\theta}\right)^n d(\sin\theta)$$

$$\left.-(\alpha\sin\theta_2+\sin\theta_4)\right] \tag{12}$$

$$h_{eq}=\frac{2A_P P_l}{\pi S}\left[\frac{n}{(n-1)\beta}(\alpha(\cos\theta_2+1)+\cos\theta_4-1)\right] \tag{13}$$

References

Barta, R.B., Ziviani, D., Groll, E.A., 2021. Design and commissioning of a modular multi-stage two-evaporator transcritical CO2 test stand. Int. J. Refrigeration 130, 392–403.

Bell, I.H., Ziviani, D., Lemort, V., et al., 2020. PDSim: A general quasi-steady modeling approach for positive displacement compressors and expanders. Int. J. Refrigeration 110, 310–322.

Choe, G., Kim, K.J., 2000. Analysis of nonlinear dynamics in a linear compressor. JSME Int. J. Ser. C 43 (3), 545–552.

Cozzolino, D., Da, L.B., Bacco, D., et al., 2019. High-dimensional quantum communication: benefits, progress, and future challenges. Adv. Quantum. Technol. 2 (12), 1970073.

Crook, M., Hills, M., Gilley, G., et al., 2021. Performance testing of a 2 K Joule-Thomson closed-cycle cryocooler. Cryocoolers 21, 433–441.

Dang, H., Zhang, L., Tan, J., 2016. Dynamic and thermodynamic characteristics of the moving-coil linear compressor for the pulse tube cryocooler. Part A: Theoretical analyses and modeling. Int. J. Refrigeration 69, 480–496.

Dang, H., Zha, R., Tan, J., et al., 2020. Investigations on a 3.3 K four-stage Stirling-type pulse tube cryocooler. Part A: Theoretical analyses and modeling. Cryogenics 105, 103014.

Dang, H., Zhang, T., Zhao, B., et al., 2022. Investigations on a 1 K hybrid cryocooler composed of a four-stage Stirling-type pulse tube cryocooler and a Joule-Thomson cooler. Part B: Experimen. Verifications. Cryogenics 123, 103452.

Liang, K., 2017. A review of linear compressors for refrigeration. Int. J. Refrigeration 84, 253–273.

Liang, K., 2018. Analysis of oil-free linear compressor operated at high pressure ratios for household refrigeration. Energy 151, 324–331.

Marquardt, E., Radebaugh, R., Kittel, P., 1992. Design equations and scaling laws for linear compressors with flexure springs. Cryocoolers 7, 783–804.

Radebaugh, R., 2009. Cryocoolers: the state of the art and recent developments. J. Phys.: Condens Matter 21 (16), 164219.

Ross Jr., R.G., 2007. Aerospace coolers: a 50-year quest for long life cryogenic cooling in space. In: Timmerhaus, K.D., Reed, R.P. (Eds.), Cryogenic Engineering: Fifty Years of Progress. Springer, New York, pp. 225–284.

Sato, Y., Sawada, K., Shinozaki, K., et al., 2016. Development of 1K-class Joule-Thomson cryocooler for next-generation astronomical mission. Cryogenics 74, 47–54.

You, L., 2020. Superconducting nanowire single-photon detectors for quantum information. Nanophotonics 9, 2673–2692.

Zhang, T., Dang, H., 2021. Investigations on a 1 K hybrid cryocooler composed of a four-stage Stirling-type pulse tube cryocooler and a Joule-Thomson cooler. Part A: Theoretical analyses and modeling. Cryogenics 116, 103282.

Zhang, X., Ziviani, D., Braun, J., et al., 2019. Numerical analysis of gas bearings in oil-free linear compressors. In: IOP Conference Series. Materials Science and Engineering, 604. IOP Publishing.

Zhao, Y., Tan, J., Zhao, B., et al., 2022. Theoretical and experimental investigations on the piston offset characteristics in a four-stage DC linear compressor unit for a 1.8 K hybrid cryocooler. Int. J. Refrigeration. https://doi.org/10.1016/j.ijrefrig.2022.11.003.

Zhu, Z., Liang, K., Chen, H., et al., 2022. Inherent capacity modulation of a linear refrigeration compressor. Int. J. Refrigeration 143, 182–191.